



Application of artificial neural networks in design of lithium-ion batteries

Bin Wu^a, Sangwoo Han^a, Kang G. Shin^b, Wei Lu^{a,*}

^a Department of Mechanical Engineering, University of Michigan, Ann Arbor, MI, 48109, USA

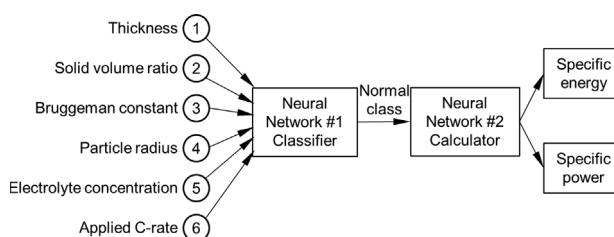
^b Department of Electrical Engineering and Computer Science, University of Michigan, Ann Arbor, MI, 48109, USA



HIGHLIGHTS

- Neural networks are constructed using data from finite element simulations.
- Neural network classifies design variables based on specific energy capability.
- Neural network predicts battery performance with negligible computational cost.
- Global sensitivity analysis is performed to identify key impact variables.
- A design map is generated to satisfy both energy and power requirements.

GRAPHICAL ABSTRACT



ARTICLE INFO

Keywords:

Lithium-ion battery
Artificial neural network
Battery design
Machine learning
Simulation

ABSTRACT

Simulation-based battery design encounters the difficulty of high computational cost. This paper presents a systematic approach based on the artificial neural network to reduce the computational burden of battery design by several orders-of-magnitude. Two neural networks are constructed using the finite element simulation results from a thermo-electrochemical model. The first neural network serves as a classifier to predict whether a set of input variables is physically feasible. The second neural network yields specific energy and specific power. Both neural networks are validated using extra finite element simulations out of the training data. With a global sensitivity analysis using the neural network, we quantify the effect of input variables on specific energy and specific power by evaluating large combinations of input variables, which is computationally prohibitive for finite element simulations. Among all parameters, the applied C-rate has the largest influence on specific power, while the electrode thickness and porosity are the dominant factors affecting specific energy. Based on this finding, we generate a design map that fulfills the requirements of both specific energy and specific power. In particular, we highlight the value of neural network in handling the non-linear, complex and computationally expensive problem of battery design and optimization.

1. Introduction

Lithium-ion batteries have been widely used in various applications, ranging from consumer electronics to electric vehicles. To satisfy the ever-growing demands for higher energy and power capability, durability and safety of batteries, the design of lithium-ion batteries has become essential to avoid any unexpected loss of performance. Battery

design based on experiments is time-consuming and expensive. In contrast, simulation-based design is not only more efficient, but also provides deeper insights into the mechanisms governing the battery performance.

Serving as a crucial step for simulation-based design, battery modeling has attracted growing interests. The majority of current battery models are based on the pseudo two-dimensional (P2D) electrochemical

* Corresponding author.

E-mail address: weilu@umich.edu (W. Lu).

model, which is based on the porous electrode theory [1]. The P2D model has been used to optimize the cathode and anode thickness, porosity, particle size and many other important electrode parameters [2–4].

The lithium-ion battery is inherently a multi-physical system. A representative example showing its multi-physical nature is the interplay between electrochemical and thermal behaviors. Heat generated by electrochemical reactions alters the temperature distribution of the electrode, which successively affects the electrochemical processes. Note that many properties of battery components, such as the electrolyte diffusivity and conductivity, are strongly related to temperature [5]. Thus, an accurate simulation often requires a thermal model to be coupled with the P2D model. In order to appropriately address the thermal effect, researchers have contributed in thermal property characterization [6], heat generation rate measurement [7] and thermo-electrochemical coupled modeling [8–10].

Despite the significant progress in the thermo-electrochemical coupled modeling of lithium-ion batteries, there remains a large gap between modeling and simulation-based design. The computational cost can be prohibitively high if a fully-coupled thermo-electrochemical model is directly applied for battery design. In simulation-based battery design, thousands of simulations are often required to determine the optimal design variables. Moreover, the complex non-linear nature of the battery model may result in convergence problems under some sets of design variables. Besides, sensitivity of the design variables is also difficult to analyze due to the very high computational cost. Without sensitivity analysis the possible reduction of design space through eliminating insensitive design variables becomes inapplicable.

Recently, artificial neural networks (ANNs, also termed simply as neural networks (NNs) when there is no ambiguity) has been shown to solve complex non-linear problems. A notable example is the application of deep neural networks in the state-of-the-art artificial intelligence of Go [11]. Loosely analogous to biological neuron systems, ANN is a computational model that consists of a large collection of connected artificial neurons. The neurons and their connections can be trained with data to represent the relations between inputs and outputs. Compared to the physical modeling, ANN has advantages in predicting the output without the knowledge of the exact information of the modeled system. Another benefit of ANN is its computational efficiency, which enables its deployment in real-time applications. ANN has been extensively used in computer science, finance, engineering and many other fields. In the field of battery the ANN approach has been explored for state-of-charge (SOC) estimation [12,13]. However, ANN has not received enough attention for battery design. Considering the potential of ANN for handling highly nonlinear complex problems with significant computational cost, we propose an approach combining the strengths of physical modeling and ANN.

The objective of this paper is to present a method of applying the neural network in simulation-based battery design. Using the simulation results from the electrochemical-thermal model as training data, we obtained two neural networks with satisfactory accuracy. The first

neural network, acted as a classifier, is used to predict whether a set of input variables is physically feasible. The second neural network is used to calculate the specific energy and specific power for any given set of input variables. These two trained neural networks are used to perform very large-scale Monte Carlo simulations, which are computationally too expensive to be achievable using the finite element method (FEM). The analysis of Monte Carlo simulation results provides many important insights in the battery design. In this paper, we first demonstrate that this neural network can be used to generate the Ragone plot, which is an important characteristic curve for electrochemical devices. Second, a global sensitivity analysis based on the Monte Carlo simulation results provides a sensitivity ranking of the input variables on specific energy and specific power. This ranking helps identify the limiting process inside the battery, thus reducing the design space. The sensitivity analysis can also help understand the influence of input inaccuracy on the outputs, thus determining the acceptable inaccuracy range for each input parameter. Finally, we characterize the battery performance with respect to most sensitive parameters, and generate a design map to satisfy the requirements of both specific energy and specific power.

2. Methodology

The first step in constructing a neural network is to determine the inputs and outputs. We are particularly interested in design variables that can be controlled in battery manufacturing. As the two most important battery performance indicators, specific energy and specific power are selected as outputs. Once the input variables are determined, we sample representative sets of variables using the design of experiments (DOE) algorithms. Using the sampled variables as inputs, a thermo-electrochemical finite element model is run to yield specific energy and specific power. The inputs and associated outputs are utilized to train the neural network. In order to validate the neural network, we compare predictions from the finite element simulation and the neural network. Once the artificial neural network is constructed with satisfactory accuracy, Monte Carlo simulations are performed for further analysis, such as the global sensitivity analysis and optimization.

2.1. Electrochemical and thermal modeling

We use the P2D model, as listed in Table 1, to resolve the solid concentration in the particle domain (the coordinate along particle radius is denoted as r), and the electrolyte concentration, electrolyte potential and solid potential in the electrode domain (the coordinate along electrode thickness is denoted as x). We denote the thickness of the negative electrode as L_n , the thickness of the separator as L_s , and the thickness of the positive electrode as L . The negative electrode, the separator and the positive electrode occupy the regions of $0 \leq x \leq L_n$, $L_n \leq x \leq L_n + L_s$, and $L_n + L_s \leq x \leq L_n + L_s + L$, respectively.

Table 1
Governing equations and boundary conditions of the electrochemical model.

Domain	Governing Equations	Boundary and Initial Conditions
Particle	$\frac{\partial c_s}{\partial t} = \frac{D_s}{r^2} \frac{\partial}{\partial r} \left(r^2 \frac{\partial c_s}{\partial r} \right)$	$r = 0: \frac{\partial c_s}{\partial r} = 0; \quad r = r_p: D_s \frac{\partial c_s}{\partial r} = -\frac{i}{F}; \quad t = 0: c_s = c_{s0}.$
Electrode	$\frac{\partial}{\partial x} \left(\sigma_s^{eff} \frac{\partial \Phi_s}{\partial x} \right) - a_s i = 0$ $\frac{\partial}{\partial x} \left(\kappa_e^{eff} \frac{\partial \Phi_e}{\partial x} + \kappa_D^{eff} \frac{\partial \ln c_e}{\partial x} \right) + a_s i = 0$ where $\kappa_D^{eff} = -\frac{2RT\kappa_e^{eff}}{F} \left(1 + \frac{d \ln f_{\pm}}{d \ln c_e} \right) (1 - t_+)$ $\varepsilon_e \frac{\partial c_e}{\partial t} = \frac{\partial}{\partial x} \left(D_e^{eff} \frac{\partial c_e}{\partial x} \right) + \frac{(1-t_+)}{F} a_s i$	$x = 0: \Phi_s = 0; \quad x = L_n: \frac{\partial \Phi_s}{\partial x} = 0;$ $x = L_n + L_s: \frac{\partial \Phi_s}{\partial x} = 0; \quad x = L_n + L_s + L: \sigma_s^{eff} \frac{\partial \Phi_s}{\partial x} = -i_{app}.$ $x = 0: \frac{\partial \Phi_e}{\partial x} = 0; \quad x = L_n + L_s + L: \frac{\partial \Phi_e}{\partial x} = 0.$
		$x = 0: \frac{\partial c_e}{\partial x} = 0; \quad x = L_n + L_s + L: \frac{\partial c_e}{\partial x} = 0; \quad t = 0: c_e = c_0.$

In Table 1, c_s is the lithium concentration in the solid (mol L^{-1}), D_s is the lithium diffusivity in the solid ($\text{m}^2 \text{s}^{-1}$), r_p is particle radius (m), F is the Faraday constant (C mol^{-1}), i is the intercalation current per unit area (A m^{-2}), c_{s0} is the initial lithium concentration in the solid (mol L^{-1}), σ_s^{eff} is the effective solid conductivity (S m^{-1}), Φ_s is the potential in the solid (V), a_s is the active surface area per unit electrode volume (m^{-3}), i_{app} is the applied current density to the electrode (A m^{-2}) with the sign defined as $i_{\text{app}} > 0$ for discharge, κ_e^{eff} is the effective electrolyte conductivity (S m^{-1}), Φ_e is the potential in the electrolyte (V), R is the gas constant ($\text{J K}^{-1} \text{mol}^{-1}$), T is temperature (K), f_{\pm} is the electrolyte activity coefficient, t_+ is the lithium ion transference number, ε_e is the electrolyte volume fraction, c_e is the lithium concentration in the electrolyte (mol L^{-1}), D_e^{eff} is the effective electrolyte diffusivity ($\text{m}^2 \text{s}^{-1}$) and c_0 is the initial lithium concentration in the electrolyte (mol L^{-1}).

The intercalation current density, i (A m^{-2}), is zero in the separator region. In the negative and positive electrode regions the current density is given by the Butler-Volmer equation,

$$i = i_0 \left(\exp\left(\frac{\beta F \eta}{RT}\right) - \exp\left(-\frac{(1-\beta)F\eta}{RT}\right) \right), \quad (1)$$

where i_0 is the exchange current density (A m^{-2}), β is the anodic charge transfer coefficient, and η is the over-potential (V) defined as

$$\eta = \Phi_s - \Phi_e - U(c_{s,\text{surf}}), \quad (2)$$

where U is the open circuit potential (V) which depends on the lithium concentration at the particle surface, $c_{s,\text{surf}}$ (mol L^{-1}). The exchange current density is given by

$$i_0 = F k c_{s,\text{surf}}^{1-\beta} c_e^\beta (c_{s,\text{max}} - c_{s,\text{surf}})^\beta, \quad (3)$$

where k is the reaction rate constant ($\text{m}^{1+3\beta} \text{mol}^{-\beta} \text{s}^{-1}$) and $c_{s,\text{max}}$ is the maximum lithium concentration in the particle (mol L^{-1}). The reaction rate constant k is assumed to follow an Arrhenius temperature-dependent relation,

$$k = k_0 \exp\left[\frac{E_{\text{act},k}}{R} \left(\frac{1}{T_0} - \frac{1}{T}\right)\right], \quad (4)$$

where $E_{\text{act},k}$ is the activation energy (kJ mol^{-1}) for k , and the subscript 0 denotes values at the reference state.

In Table 1, the active surface area per unit electrode volume (m^{-1}) is given by $a_s = \frac{3\varepsilon}{r_p}$, where ε is the solid volume fraction. The effective solid conductivity, effective electrolyte diffusivity and effective electrolyte conductivity are given as

$$\sigma_s^{\text{eff}} = \sigma_s \frac{\varepsilon}{\tau}, \quad D_e^{\text{eff}} = D_e \frac{\varepsilon_e}{\tau_e}, \quad \kappa_e^{\text{eff}} = \kappa_e \frac{\varepsilon_e}{\tau_e}, \quad (5)$$

where σ_s is the solid bulk conductivity (S m^{-1}), τ is the solid tortuosity, D_e and κ_e are the bulk electrolyte diffusivity ($\text{m}^2 \text{s}^{-1}$) and conductivity (S m^{-1}), ε_e is the electrolyte volume fraction and τ_e is the electrolyte tortuosity. The tortuosity of the solid and the electrolyte are given by the Bruggeman relation,

$$\tau = \varepsilon^{1-\alpha}, \quad \tau_e = \varepsilon_e^{1-\alpha}, \quad (6)$$

where α is the Bruggeman constant. Typically, α is set as 1.5 in battery simulations. However, recent reports [14–16] reveal that α may have different values. In this paper, we will investigate the effect of α on battery performance. The electrolyte bulk conductivity and diffusivity are functions of temperature and concentration, which are adopted from Ref. [5].

As the reaction constant, the electrolyte diffusivity and conductivity depend on temperature, accurate modeling requires a full coupling of thermal and electrochemical behaviors. The temperature of the electrode is governed by

$$\rho C_p \frac{\partial T}{\partial t} = K \frac{\partial^2 T}{\partial x^2} + q, \quad (7)$$

where ρ is the density (kg m^{-3}), C_p is the specific heat capacity ($\text{J kg}^{-1} \text{K}^{-1}$), K is the thermal conductivity ($\text{W m}^{-1} \text{K}^{-1}$), and the heat generation rate q (W m^{-3}) is given by

$$q = a_s i (\Phi_s - \Phi_e - U) + a_s i T \frac{\partial U}{\partial T} + \sigma_s^{\text{eff}} \left(\frac{\partial \Phi_s}{\partial x}\right)^2 + \kappa_e^{\text{eff}} \left(\frac{\partial \Phi_e}{\partial x}\right)^2 + \kappa_D^{\text{eff}} \left(\frac{\partial \ln c_e}{\partial x}\right) \left(\frac{\partial \Phi_e}{\partial x}\right). \quad (8)$$

The thermal boundary condition is given by

$$K \frac{\partial T}{\partial x} = h(T - T_0) \quad \text{at } x = 0, \\ -K \frac{\partial T}{\partial x} = h(T - T_0) \quad \text{at } x = L_n + L_s + L, \quad (9)$$

where T_0 is the environmental temperature (K) as well as the initial temperature of the cell setting at 25 °C, and h is the heat convection coefficient ($\text{W m}^{-2} \text{K}^{-1}$).

We implemented the thermo-electrochemical model using the finite element software package COMSOL Multiphysics. The finite element method has been widely used for solid structure, heat transfer, fluid dynamics and mass transfer calculations. It is now playing an important role in battery modeling and analysis. In particular, the material properties in the finite element method are defined element-wise. Therefore, the material properties can be spatial-dependent, being different from element to element, and they can also depend on other variables. Thus natural material properties can be taken account of [6,9,10,15]. For instance, diffusivity depends on temperature and therefore each element will have different values [9]. Such dependence can be easily defined in COMSOL by an equation or a table.

2.2. Inputs

The first step in design optimization is to determine the appropriate input variables and their ranges. Our focus in this paper is on the variables that are controllable during battery manufacturing. Specifically, this paper focuses on the positive electrode. The inherent properties, such as diffusivity and conductivity, are constants for a given material. The positive electrode thickness, positive solid phase volume fraction, positive Bruggeman constant and positive active material particle radius and C-rate are chosen as the input variables.

Among all the design variables, the electrode thickness, solid phase volume fraction and particle radius are easy to control in battery manufacturing. The initial electrolyte concentration is another important and tunable variable. Generally, this variable is set as 1 mol L^{-1} , where the maximum conductivity can be reached [17]. However, this concentration may lead to local electrolyte dry-up, which may decrease available energy or even accelerate capacity degradation. This effect has been found in both simulations and experiments [18], highlighting the benefits of high initial concentration. In this paper, we prescribe three levels of initial electrolyte concentrations to explore the effect of initial electrolyte concentration.

The Bruggeman constant is not a directly controllable variable. Physically, the tortuosity of two electrodes can be different even when the volume fraction is the same. The Bruggeman constant can be regarded as a variable characterizing the electrode microstructure. In addition, while most prior studies assume that this constant is 1.5, we are interested in whether this assumption has a major influence on the simulation results.

The applied C-rate, although an operational variable rather than a design variable, is also selected as an input variable. The primary reason is that the battery performance is usually evaluated at several C-rates. Thus, the neural network should provide the capability to adjust the C-rate. The applied C-rate can be related to the current density by

Table 2
Design variables and their ranges.

Variable	Symbol (Unit)	Range
Positive electrode thickness	L (μm)	50–130
Positive solid phase volume fraction	ε	0.5–0.8
Positive Bruggeman constant	α	1.5–2.0
Positive active material particle radius	r_p (μm)	3–12
Electrolyte Li^+ concentration	c_0 (mol L^{-1})	0.8, 1, 1.2
Applied C-rate	C-rate (h^{-1})	C/2, 1C, 3C

$$i_{app} = C\text{-rate} \times L\varepsilon Q_p, \quad (10)$$

where Q_p is the volumetric capacity of the positive electrode active material.

Table 2 lists the 6 design variables and their ranges. After determining the design variables, 900 sets of design-of-experiment variables are generated based on the Latin hypercube design (LHD) algorithm and the face centered composite design (FCCD) algorithm [19].

In this paper, the positive electrode is $\text{Li}_x\text{Ni}_{1/3}\text{Co}_{1/3}\text{Mn}_{1/3}\text{O}_2$ (NCM) and the negative electrode is Li_xC_6 . The capacity ratio of the negative electrode over the positive electrode, R_{np} , is kept at a constant of 1.05. A ratio slightly larger than 1 is chosen in order to ensure the full utilization of the more expensive positive electrode active material, as well as to avoid overlithiation and lithium plating.

$$R_{np} = \frac{Q_n L_n \varepsilon_n}{Q_p L \varepsilon} = 1.05, \quad (11)$$

where Q_n is the volumetric capacity of the negative electrode active material and ε_n is the volume fraction of the negative electrode active material. Given L and ε , the thickness and solid volume fraction of the negative electrode are given as

$$L_n = \frac{L}{1.15}, \quad \varepsilon_n = \frac{\varepsilon}{1.086}. \quad (12)$$

Table 3 lists the parameters for the electrochemical-thermal model.

Table 3
Input parameters for the coupled electrochemical-thermal model.

Parameters (Unit)	Positive electrode	Negative electrode	Separator	Entire cell
Dimensional & microstructural parameters				
Thickness (μm)	L	$L/1.15$	20	–
Solid phase volume fraction	ε	$\varepsilon/1.086$	0.61	–
Bruggeman constant	α	α	2.6	–
Particle radius (μm)	r_p	8	–	–
Cell projected area, A (m^2)	–	–	–	0.01
Thermodynamic parameters				
Volumetric capacity, Q_p, Q_n (mA h cm^{-3})	562	737	–	–
Open circuit voltage, U (V)	Ranging from 2.6 to 4.7, Ref. [20]	Ranging from 0.1 to 1.2, Ref. [21]	–	–
Entropy coefficient, $\partial U/\partial T$ (V K^{-1})	Ranging from	Ranging from	–	–
-1.3×10^{-4} to -6×10^{-5} , Ref. [22]	-6×10^{-4} to	6×10^{-4} , Ref. [21]	–	–
Transport parameters				
Solid diffusivity, D_s ($\text{m}^2 \text{s}^{-1}$)	1×10^{-13}	1×10^{-13}	–	–
Solid electrical conductivity, σ_s (S m^{-1})	0.1	100	–	–
Electrolyte diffusivity, D_e ($\text{m}^2 \text{s}^{-1}$)	Function of T and c_e , ranging from 2×10^{-10} to 1×10^{-9} , Ref. [5]	–	–	–
Electrolyte conductivity, κ_e (S m^{-1})	Function of T and c_e , ranging from 0 to 1.7, Ref. [5]	–	–	–
Mean molar activity, $1 + \frac{d \ln f_{\pm}}{d \ln c_e}$	Function of T and c_e , ranging from 1 to 15, Ref. [5]	–	–	–
Kinetic parameters				
Reaction rate constant at 25 °C, k_0 ($\text{m}^{2.5} \text{mol}^{0.5} \text{s}^{-1}$)	6.15×10^{-11}	6.15×10^{-11}	–	–
Reaction activation energy, $E_{act,k}$ (kJ mol^{-1})	30	30	–	–
Anodic charge transfer coefficient, β	0.5	0.5	–	–
Thermal parameters				
Specific heat capacity, C_p ($\text{J kg}^{-1} \text{K}^{-1}$)	900	1437	1978	–
Thermal conductivity, K ($\text{W m}^{-1} \text{K}^{-1}$)	5	5	1	–
Heat convection coefficient, h ($\text{W m}^{-2} \text{K}^{-1}$)	–	–	–	5

2.3. Outputs

The objective functions of the simulation-based design involve specific energy and specific power, which are defined as

$$E = \frac{\int_0^{t_d} IV dt}{m}; \quad (13)$$

$$P = \frac{\int_0^{t_d} IV dt}{m t_d}, \quad (14)$$

where $I = i_{app}A$ is the applied discharge current, A is the cell projected area given in Table 3, V is the voltage profile given by the finite element simulation, t_d is the discharge time when V hits the low voltage threshold of 2.5 V, and m is the cell mass.

The cell mass is the sum of the current collectors, separator and electrodes,

$$m = A \left(\rho_{Al} d_{Al} + \sum_{i \in \text{pos}} \rho_i \varepsilon_i d_{\text{pos}} + \sum_{i \in \text{sep}} \rho_i \varepsilon_i d_{\text{sep}} + \sum_{i \in \text{neg}} \rho_i \varepsilon_i d_{\text{neg}} + \rho_{Cu} d_{Cu} \right), \quad (15)$$

where ρ is the density, d is the thickness and ε is the volume fraction. As the positive electrode consists of active particles, electrolyte, binder and additives, the mass of the positive electrode is the sum of those phases. The summation also applies for the separator and the negative electrode. The parameters needed in Eq. (15) are listed in Table 4.

2.4. Neural network construction

The simulation results from the electrochemical and thermal modeling provide the training data to construct neural network that correlate the inputs and outputs. Physically, some sets of inputs may lead to “abnormal” outputs, such as significantly low specific energy because of local depletion of electrolyte, which prevents lithium transport. The “abnormal” results occur when the combination of input parameters are outside of the range for sustaining intercalation or deintercalation. The accuracy of neural network in calculating outputs will be diminished if

Table 4
Density, volume fraction and thickness of the components inside the battery.

	Density	Volume fraction	Thickness
Al current collector	2707 kg m ⁻³	1	25 μm
Positive electrode			
Active particle (NCM)	4210 kg m ⁻³	ϵ	L
Binder and additive	1800 kg m ⁻³	0.1	
Electrolyte	1324 kg m ⁻³	1-0.1- ϵ	
Separator			
PP	855 kg m ⁻³	0.61	20 μm
Electrolyte	1324 kg m ⁻³	0.39	
Negative electrode			
Active particle (LiC ₆)	2200 kg m ⁻³	$\epsilon/1.086$	$L/1.15$
Binder and additive	1800 kg m ⁻³	0.1	
Electrolyte	1324 kg m ⁻³	1-0.1- $\epsilon/1.086$	
Cu current collector	8954 kg m ⁻³	1	25 μm

the training data contain those “abnormal” results since they cause a sharp discontinuity of system behavior. Our solution to this problem is to introduce another neural network, which acts as a *classifier* to judge whether a set of inputs is normal or abnormal. The *calculator* neural network performs calculation only for inputs which are classified by the *classifier* neural network as normal. Thus, the *classifier* neural network is trained using the whole sets of inputs, while the *calculator* neural network is trained using only normal sets of inputs.

The *classifier* and *calculator* neural networks are both constructed using the MATLAB Neural Network Toolbox. As shown in Fig. 1(a), the input vector is six-dimensional, representing the six input variables, while the output is a value ranging from 0 to 1. The value 0 represents abnormal while the value 1 represents normal. The hidden layer between the input and the output consists of 10 neurons, which has been proven sufficient for our applications. The symbol “*w*” represents weight and “*b*” represents bias. The transfer function in the hidden layer is the sigmoid function while the transfer function in the output layer is the softmax function. Fig. 1(b) shows the schematic of the *calculator* artificial neural network. Similar to Fig. 1(a), the input vector is six-dimensional, representing the six input variables, while the output vector is two-dimensional, representing specific energy and specific power. The hidden layer between the input and the output consists of 10 neurons with the sigmoid transfer function. The output layer has a linear transfer function. The training data for this neural network come from the FEM simulation results classified as normal by the *classifier* neural network.

With the trained neural networks, we performed 10000 sets of Monte Carlo simulations, which are computationally prohibitive for the finite element method. These simulations provide the global sensitivity of each input on the output. The details can be found in Section 3.3. The sensitivity analysis results help to narrow down the battery design

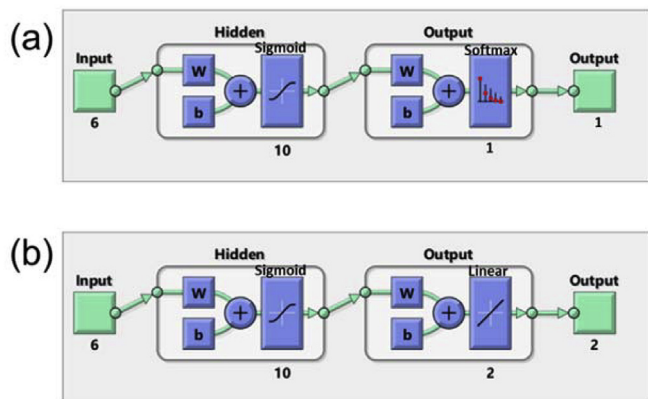


Fig. 1. (a) Schematic of the *classifier* neural network. (b) Schematic of the *calculator* neural network.

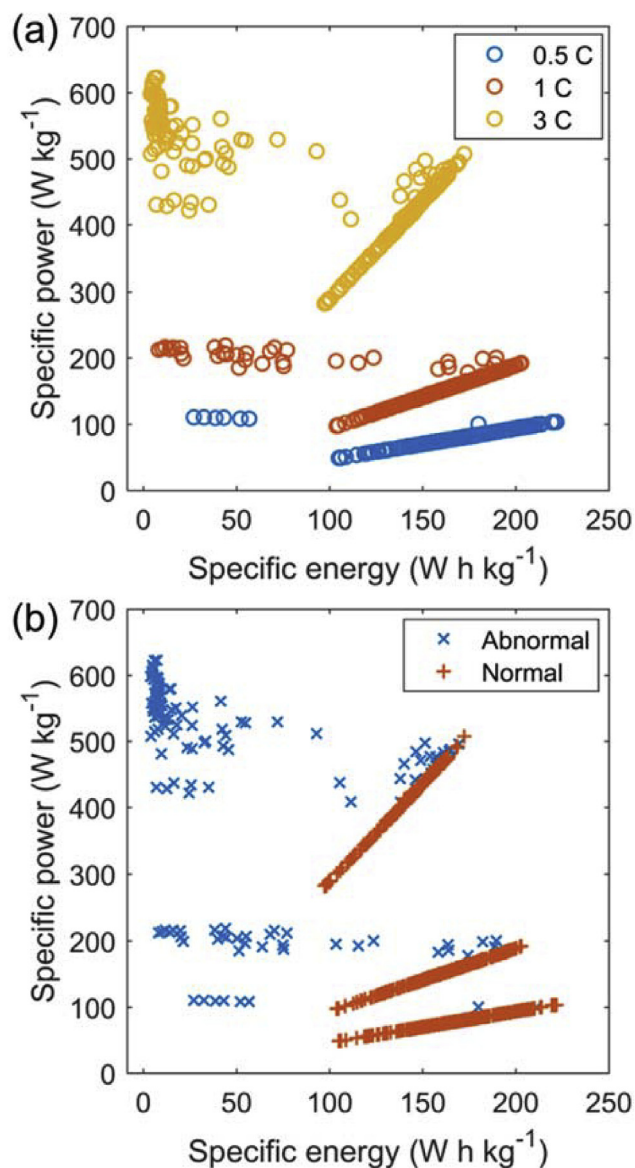


Fig. 2. Specific power with respect to specific energy from finite element simulations of the electrochemical-thermal model. (a) The color of the dot represents the applied C-rate. (b) The color and symbol represents the normal or abnormal simulations. (For interpretation of the references to color in this figure legend, the reader is referred to the Web version of this article.)

space by eliminating the insensitive design variables. In the refined design space, the neural networks generate a design map relating sensitive design variables with specific energy and specific power. The details of battery performance optimization can be found in Section 3.4.

3. Results and discussion

3.1. Classifier neural network

Fig. 2(a) shows the specific energy and specific power obtained from FEM simulations of the electrochemical-thermal model with the 900 sets of input variables. Each dot represents a set of input variables, and the color illustrates the C-rate. What stands out in Fig. 2(a) is that tens of simulations deliver negligible specific energy. Closer investigation reveals that those simulations abruptly terminate when the electrolyte concentration in the positive electrode drops below 0.001 mol L⁻¹ because electrolyte concentration cannot further decrease to negative

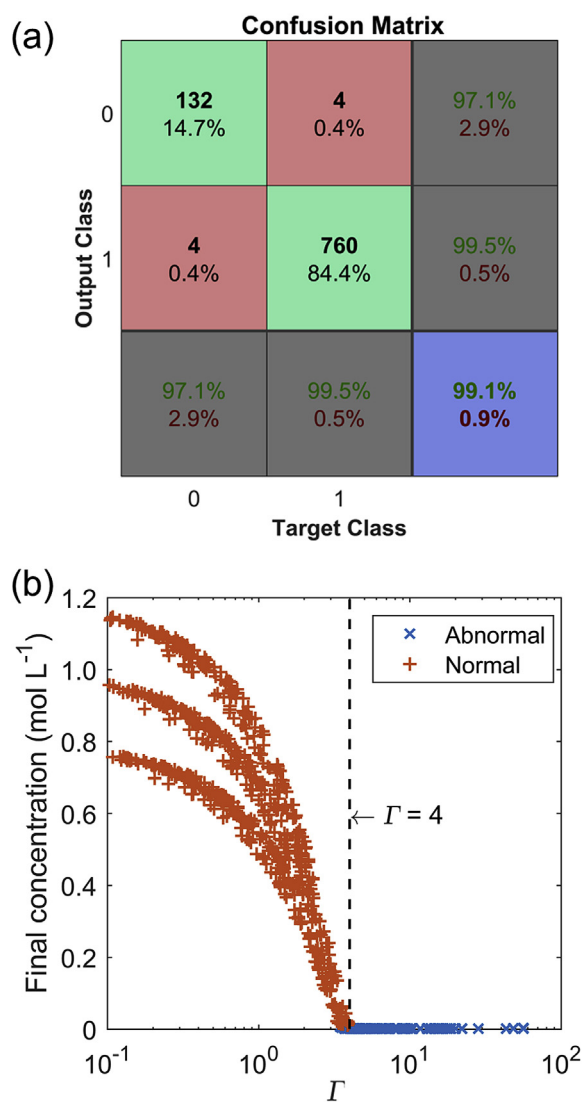


Fig. 3. (a) Confusion matrix of neural network-based classifier. (b) Relation between Γ and the minimum electrolyte concentration of positive electrode at the end of discharge.

during the simulation of discharge. The depletion of electrolyte brings physical implications. The dry up of electrolyte can lead to the loss of electrochemical activity in local regions, which may further grow because of the particle interaction effect [23]. Consequently, we are interested in avoiding input variables that may result in the depletion of electrolyte. In the following text, the simulation that results in very low electrolyte concentration ($< 0.01 \text{ mol L}^{-1}$) at the final instant is termed as abnormal. Fig. 2(b) shows the classified normal and abnormal simulations. Note that some abnormal simulations may still give considerable specific energy, as those simulations proceed to discharge until reaching a very low final electrolyte concentration.

Then, we look at using the *classifier* neural network to separate abnormal simulations, which can be regarded as a typical classifier problem in machine learning. The abnormal cases in Fig. 2(a) are tagged as Class 0, while the remaining normal cases are tagged as Class 1. The 900 sets of input variables and their resulting classes are used to train a neural network-based classifier. The confusion matrix in Fig. 3(a) visualizes the performance of this neural network. The target class represents the actual class, while the output class represents the class predicted by the neural network. Of the 900 cases, the neural network correctly predicts 760 cases of Class 1 (among 764 cases) and 132 cases of Class 0 (among 136 cases). The false positive rate is 2.9%

and the false negative rate is 0.5%. The accuracy of each target class and output class can be found in the gray grid. Overall, the accuracy of the trained neural network is $(760 + 132)/900 = 99.1\%$ as shown in the blue grid.

The results from the *classifier* neural network motivate us to consider whether there exists a physical characteristic number to separate the normal and abnormal cases. Physically, the electrolyte lithium concentration in the positive electrode decreases due to the intercalation of lithium ions into positive electrode active particles. Meanwhile, lithium ions diffuse across the separator to replenish the consumed lithium ions. Thus, a non-dimensional characteristic number can be used to compare the two effects,

$$\Gamma = \frac{i_{app}/F}{D_e^{eff} c_0/L} = \frac{i_{app}L}{FD_e^{eff} c_0}, \quad (16)$$

where i_{app}/F can be regarded as the lithium consumption rate required by the applied current and $D_e^{eff} c_0/L$ can be regarded as the electrolyte supply rate due to diffusion. As shown in Fig. 3(b), $\Gamma = 4$ serves as a satisfying threshold to determine whether a simulation is abnormal or normal. The input variables yielding $\Gamma > 4$ generally result in very low final electrolyte concentration, and thus abnormal simulations. This is a rather remarkable outcome as Γ can be calculated without running the computationally expensive simulation.

In order to further evaluate the performance of the characteristic number and the neural network, we conducted 11 more simulations. Note that the 11 simulations are not included in the previous 900 simulations. In Fig. 4(a), the threshold of $\Gamma = 4$ successfully separates the normal and abnormal cases. The prediction from the neural network is a value ranging from 0 to 1, while the value of 0.5 can be used as the threshold in Fig. 4(b). The results in Fig. 4 show that both the characteristic number and the neural network work well in telling whether a simulation is normal or abnormal. It is interesting to further compare the two approaches. First, we note that Γ calculated in Eq. (16) can only represent the initial state. However, a significant temperature increase in cold environments leads to salient change in electrolyte diffusivity, making Γ not representative of the whole discharging course. This thermal effect may diminish the usefulness of Γ . Second, although this paper only considers the depletion of electrolyte as the sole reason for abnormal simulations, other factors may become important under different ranges of inputs. For example, the slow solid diffusion may lead to over-lithiation or over-delithiation for large particles with low diffusivity. In this regard, various characteristic numbers should be proposed to describe the different limiting processes. In contrast, the neural network approach provides a unified framework to classify the abnormal simulations.

3.2. Calculator neural network

This section focuses on the calculation of specific energy and specific power using the neural network. The construction of the *calculator* neural network can be found in Section 2.4.

To validate the constructed neural network, we compare the Ragone plots from the neural network and finite element simulations. Providing the relation between specific energy and specific power, Ragone plot has been widely used to characterize the performance of energy storage devices [24,25]. As shown in Fig. 5, the Ragone plots from the neural network agree well with the finite element simulations, meanwhile the computational cost is greatly reduced. Note that the input variables for this validation are out of the training dataset. Each FEM dot in Fig. 5 takes about 6 min of computation, thus the FEM simulations can only be performed at several discrete C-rates due to the computational cost. The orange dots in Fig. 5 take a total of 3 h of computation. In contrast, it takes less than 1 s for the *calculator* neural network to generate the entire continuous curve. This dramatic acceleration of calculation by several orders of magnitude highlights the great value of neural

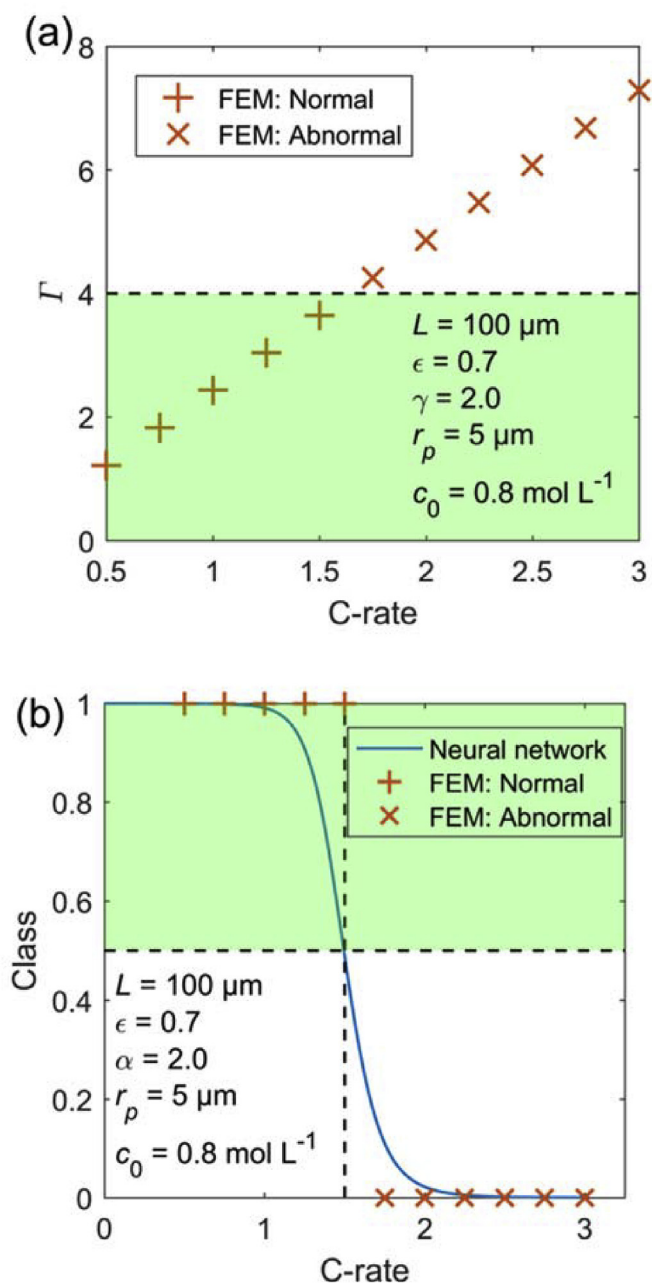


Fig. 4. Comparison between electrochemical-thermal simulations based on the finite element method (FEM) and (a) non-dimensional characteristic number, (b) neural network-based classifier. The green region denotes the normal area. Five of the design variables are kept constant as shown in the figure, while the C-rate changes from 0.5 C to 3 C. (For interpretation of the references to color in this figure legend, the reader is referred to the Web version of this article.)

network in battery design applications.

3.3. Global sensitivity analysis

Given a generic model $Y = f(X_1, X_2, \dots, X_k)$, sensitivity analysis provides a systematic approach to quantify the influence of input X_i on the output Y . Two main categories of sensitivity analysis have been proposed in the literature. The local sensitivity analysis is based on the derivative $\partial Y / \partial X_i$. Although having the attraction of being computationally efficient, this approach can only provide information at specific points where the derivative is calculated. Thus, the derivative-based local sensitive analysis is unwarranted when the model inputs are

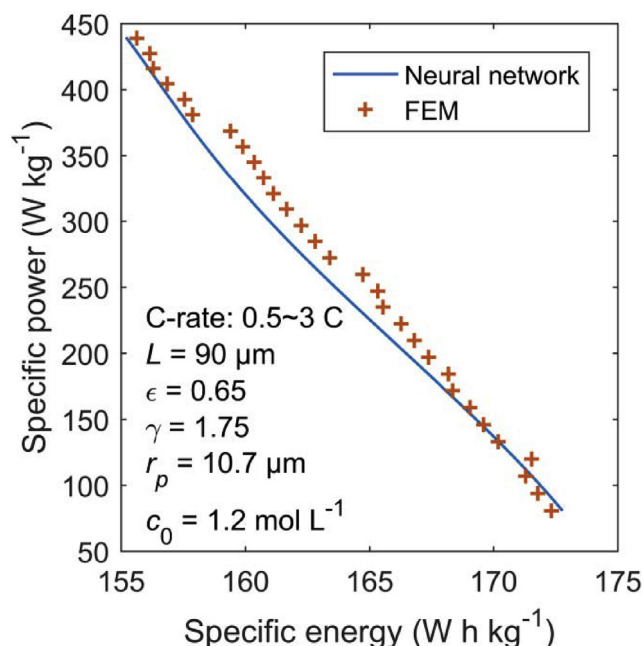


Fig. 5. Ragone plots from neural network calculations and electrochemical-thermal simulations based on the finite element method (FEM). Each FEM dot represents a finite element simulation. Five of the design variables are kept constant as shown in the figure, while the C-rate changes from 0.5C to 3C.

highly uncertain or when the model is non-linear in nature. In contrast, global sensitivity analysis can provide comprehensive information over the whole input range even when the model is nonlinear [26]. Based on the variation decomposition principle [26,27], the first order global sensitivity is defined as

$$S_i = \frac{V[E(Y|X_i)]}{V(Y)}, \quad (17)$$

where $E(Y|X_i)$ is the conditional expectation over each X_i , and $V(\cdot)$ stands for variance. Intuitively, $E(Y|X_i)$ can be calculated by cutting the input domain into X_i slices and averaging Y over each slice. If this conditional expectation has a large variation across X_i , then this factor is regarded as important. The first order sensitivity essentially represents the fraction of output variance that can be explained by considering the input X_i alone [28]. Notably, global sensitivity analysis can also be used to explore the possible interaction effect among inputs. More details can be found in Ref. [29].

Fig. 6 shows the first order sensitivity of the six input variables on specific energy and specific power. The electrode thickness and porosity are the dominant factors affecting specific energy. In contrast, the applied current density is the decisive factor on specific power. The salient effect of C-rate on specific power can also be found in Fig. 2. Another observation from Fig. 6 is that the initial electrolyte concentration, the Bruggeman constant and the particle radius have minor influence on both specific energy and specific power. Thus, we keep these factors as constant in the following optimization section.

3.4. Optimization

Another application of the constructed neural networks is to optimize the battery design. As the initial electrolyte concentration, the Bruggeman constant and the particle radius have negligible influence on specific energy and specific power, we focus on the optimization of the electrode thickness and the solid volume fraction in this section.

As the practical application often requires a specific current density instead of C-rate, we prescribe a constant current density of 60 A m^{-2} in the optimization. The C-rate can be calculated from the applied

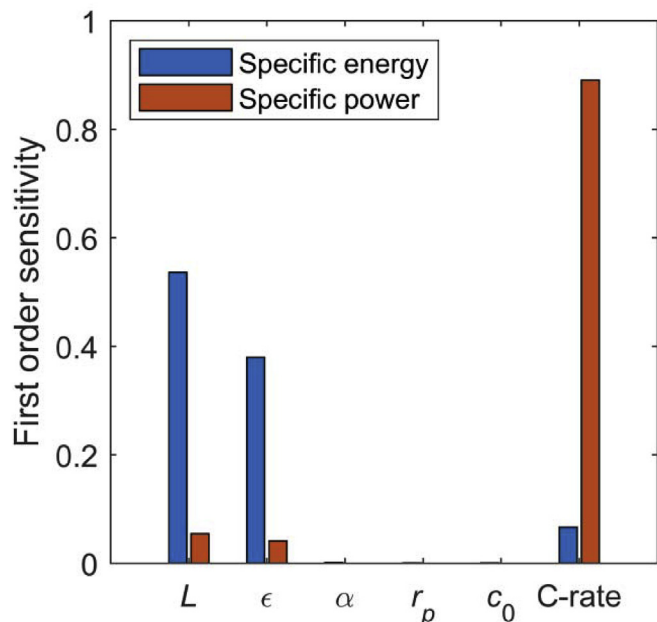


Fig. 6. First order sensitivity of the six input variables on specific energy and specific power.

current density using Eq. (10).

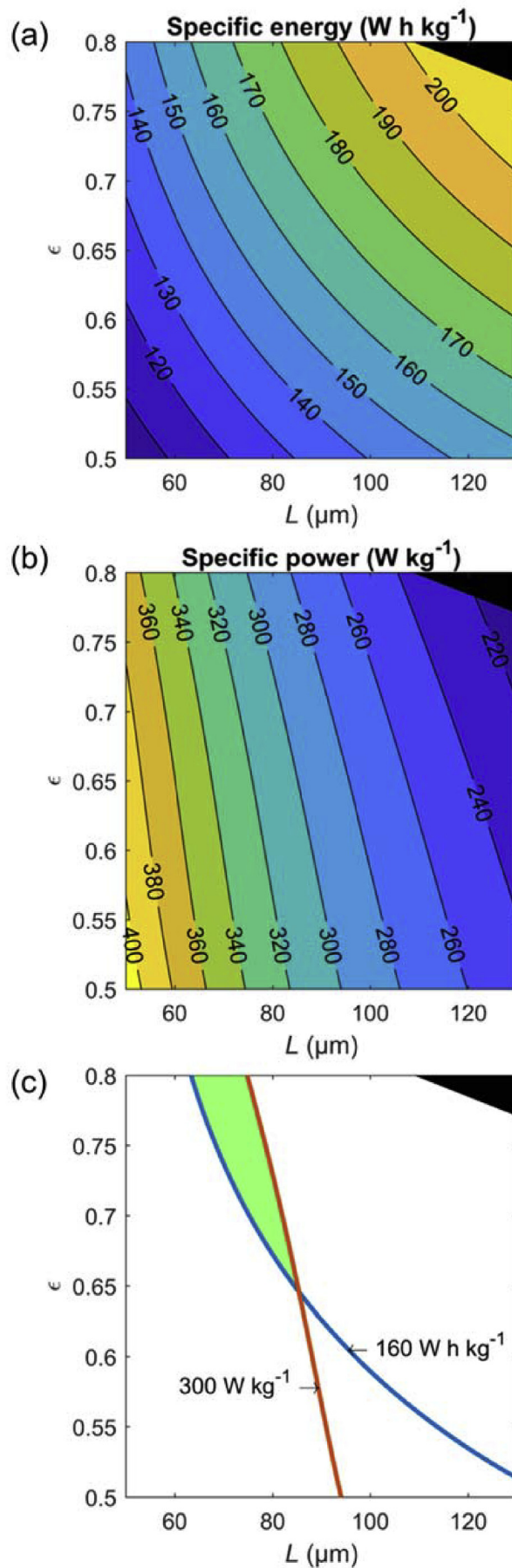
The first step is to distinguish the infeasible design regions, where the simulations may be abnormal. Using the *classifier* neural network developed in 3.1, the input is judged as infeasible when the predicted class value is lower than 0.5. As a result, the infeasible region is shown black in Fig. 7.

Using the *calculator* neural network, the specific energy and specific power with respect to the electrode thickness and the solid volume fraction are shown in Fig. 7. Thick electrode and high volume fraction of active materials lead to high specific energy at the cost of low specific power. These results coincide with current battery design principles: the energy-type batteries (used for high-energy applications, such as pure electric vehicles) usually have thick and dense electrodes, while the power-type batteries (used for high-power applications, such as hybrid electric vehicles) are associated with thin and porous electrodes. The contours of Fig. 7(a) and (b) can be combined to fulfill both requirements of specific energy and specific power. As shown in Fig. 7(c), the green area denotes the feasible region where the specific energy is larger than 160 Wh kg^{-1} and the specific power is larger than 300 W kg^{-1} .

4. Conclusions

The high computational cost of coupled electrochemical-thermal model has prevented its utilization in the simulation-based battery design. In this paper, we demonstrated that neural networks are highly valuable for battery design, reducing the computational burden by several orders-of-magnitude. Two neural networks have been constructed, trained and validated using the data from finite element simulations. The first neural network, the *classifier*, was used to predict whether a set of input variables is physically feasible. The second neural network, the *calculator*, was used to calculate specific energy and specific power. Comparison between the neural networks and finite element simulations demonstrated that both the two neural networks achieved satisfying accuracy.

Using the neural networks, many computationally expensive analyses can be performed with negligible computational cost. As an example, a continuous Ragone plot was generated, which was in good agreement with the discrete Ragone plot from finite element



(caption on next page)

Fig. 7. Design map generated with neural network. (a) Specific energy contour with respect to the positive electrode thickness and the positive electrode solid volume fraction. (b) Specific power contour with respect to the positive electrode thickness and the positive electrode solid volume fraction. (c) Application of the contours to determine the design area. The green region denotes the feasible region satisfying both requirements of specific energy and specific power. In all figures, the black region denotes the infeasible region where the Class predicted by the classifier neural network is less than 0.5. Other inputs to the neural network are $i_{app} = 60 \text{ A m}^{-2}$, $\alpha = 1.5$, $r_p = 5 \mu\text{m}$, $c_0 = 1 \text{ mol L}^{-1}$. (For interpretation of the references to color in this figure legend, the reader is referred to the Web version of this article.)

simulations. Moreover, we performed global sensitivity analysis to rank the sensitivity of input variables on specific energy and specific power. We found that the applied C-rate is the dominant factor affecting specific power, while the electrode thickness and porosity are most significant input variables for specific energy. Based on this finding, we obtained contours that characterize the specific energy and specific power with respect to the most important variables. Finally, a design map was generated to fulfill the requirements of both specific energy and specific power. Although this paper is focused on the NCM and graphite electrodes, the developed method can be easily generalized to other active materials. Moreover, the materials selection can also be used as an input for the neural networks. With high computational efficiency, the developed neural networks can potentially be extended to other battery applications such as advanced battery management systems for real time control.

Acknowledgement

This work was supported in part by the National Science Foundation under Grant No. CNS-1446117.

References

[1] M. Doyle, T.F. Fuller, J. Newman, *J. Electrochem. Soc.* 140 (1993) 1526–1533.

- [2] N.S. Xue, W.B. Du, A. Gupta, W. Shyy, A.M. Sastry, J.R.R.A. Martins, *J. Electrochem. Soc.* 160 (2013) A1071–A1078.
- [3] S. De, P.W.C. Northrop, V. Ramadesigan, V.R. Subramanian, *J. Power Sources* 227 (2013) 161–170.
- [4] V. Ramadesigan, R.N. Methekar, F. Latinwo, R.D. Braatz, V.R. Subramanian, *J. Electrochem. Soc.* 157 (2010) A1328–A1334.
- [5] L.O. Valoen, J.N. Reimers, *J. Electrochem. Soc.* 152 (2005) A882–A891.
- [6] J.B. Zhang, B. Wu, Z. Li, J. Huang, *J. Power Sources* 259 (2014) 106–116.
- [7] J.B. Zhang, J. Huang, Z. Li, B. Wu, Z.H. Nie, Y. Sun, F.Q. An, N.N. Wu, *J. Therm. Anal. Calorim.* 117 (2014) 447–461.
- [8] W.B. Gu, C.Y. Wang, *J. Electrochem. Soc.* 147 (2000) 2910–2922.
- [9] L. Liu, J. Park, X.K. Lin, A.M. Sastry, W. Lu, *J. Power Sources* 268 (2014) 482–490.
- [10] B. Wu, Z. Li, J.B. Zhang, *J. Electrochem. Soc.* 162 (2015) A181–A191.
- [11] D. Silver, A. Huang, C.J. Maddison, A. Guez, L. Sifre, G. van den Driessche, J. Schrittwieser, I. Antonoglou, V. Panneershelvam, M. Lanctot, S. Dieleman, D. Grewe, J. Nham, N. Kalchbrenner, I. Sutskever, T. Lillicrap, M. Leach, K. Kavukcuoglu, T. Graepel, D. Hassabis, *Nature* 529 (2016) 484–489.
- [12] S. Piller, M. Perrin, A. Jossen, *J. Power Sources* 96 (2001) 113–120.
- [13] T. Weigert, Q. Tian, K. Lian, *J. Power Sources* 196 (2011) 4061–4066.
- [14] T. DuBeshter, P.K. Sinha, A. Sakars, G.W. Fly, J. Jorne, *J. Electrochem. Soc.* 161 (2014) A599–A605.
- [15] W.B. Du, N.S. Xue, W. Shyy, J.R.R.A. Martins, *J. Electrochem. Soc.* 161 (2014) E3086–E3096.
- [16] I.V. Thorat, D.E. Stephenson, N.A. Zacharias, K. Zaghbi, J.N. Harb, D.R. Wheeler, *J. Power Sources* 188 (2009) 592–600.
- [17] Y. Yamada, A. Yamada, *J. Electrochem. Soc.* 162 (2015) A2406–A2423.
- [18] J. Mao, W. Tiedemann, J. Newman, *J. Power Sources* 271 (2014) 444–454.
- [19] R.H. Myers, D.C. Montgomery, C.M. Anderson-Cook, *Response Surface Methodology: Process and Product Optimization Using Designed Experiments*, Wiley and Sons Inc., New York, 1995.
- [20] N. Yabuuchi, Y. Makimura, T. Ohzuku, *J. Electrochem. Soc.* 154 (2007) A314–A321.
- [21] Y.F. Reynier, R. Yazami, B. Fultz, *J. Electrochem. Soc.* 151 (2004) A422–A426.
- [22] W. Lu, I. Belharouak, D. Vissers, K. Amine, *J. Electrochem. Soc.* 153 (2006) A2147–A2151.
- [23] B. Wu, W. Lu, *J. Power Sources* 360 (2017) 360–372.
- [24] T. Christen, M.W. Carlen, *J. Power Sources* 91 (2000) 210–216.
- [25] D.V. Ragone, Mid-year Meeting of the Society of Automotive Engineers, Detroit, MI, 1968.
- [26] A. Saltelli, M. Ratto, T. Andres, F. Campolongo, J. Cariboni, D. Gatelli, M. Saisana, S. Tarantola, *Global Sensitivity Analysis, The Primer*, John Wiley & Sons, 2008.
- [27] I.M. Sobol, *Math. Comput. Simulat.* 55 (2001) 271–280.
- [28] W.B. Du, A. Gupta, X.C. Zhang, A.M. Sastry, W. Shyy, *Int. J. Heat Mass Tran.* 53 (2010) 3552–3561.
- [29] F. Cannavo, *Comput. Geosci. Uk* 44 (2012) 52–59.